Formation of buckminsterfullerene (C_{60}) in interstellar space

Olivier Berné[1] and A. G. G. M. Tielens

Leiden Observatory, Leiden University, P.O. Box 9513, NL- 2300 RA Leiden, The Netherlands

Edited by Neta A. Bahcall, Princeton University, Princeton, NJ, and approved November 2, 2011 (received for review August 31, 2011)

Buckminsterfullerene (C_{60}) was recently confirmed as the largest molecule identified in space. However, it remains unclear how and where this molecule is formed. It is generally believed that C_{60} is formed from the buildup of small carbonaceous compounds in the hot and dense envelopes of evolved stars. Analyzing infrared observations, obtained by Spitzer and Herschel, we found that C_{60} is efficiently formed in the tenuous and cold environment of an interstellar cloud illuminated by strong ultraviolet (UV) radiation fields. This implies that another formation pathway, efficient at low densities, must exist. Based on recent laboratory and theoretical studies, we argue that polycyclic aromatic hydrocarbons are converted into graphene, and subsequently C_{60}, under UV irradiation from massive stars. This shows that alternative—top-down—routes are key to understanding the organic inventory in space.

fullerene | interstellar medium

The midinfrared spectra of a variety of astrophysical objects are dominated by band emission (strongest at 3.3, 6.2, 7.7, 8.6, and 11.2 μm) attributed to carbonaceous macromolecules [i.e., polycyclic aromatic hydrocarbons (PAHs)] (1). These molecules are large (30–100 C atoms), abundant (approximately 5% of the elemental carbon), and their ionization plays a key role in the energy balance of gas in the interstellar medium (ISM) and in protoplanetary disk. In addition to PAH bands, infrared signatures observed at 7.0, 8.5, 17.4, and 19.0 μm have been reported recently (2, 3) and found to coincide precisely with the emission of buckminsterfullerene (C_{60}) (4), a cage-like carbon molecule. This detection heralds the presence of a rich organic inventory and chemistry in space. However, observed abundances of C_{60} challenge the standard ion-molecule or grain-surface chemistry formation routes, which build up molecules from small to large in the ISM. For that reason, it has been suggested that C_{60} is formed in the hot and dense envelopes of evolved stars (5–7) in processes similar to those found in sooty environments (8–11), and eventually, is ejected in space. Yet, this scenario faces the problem that it has a limited efficiency (6). PAHs and C_{60} are known to coexist in the ISM (3); however, so far, the connection between PAHs and C_{60}—and in particular the possibility to go from one compound to the other in space—has not been investigated. In this paper, we present a study of PAH and C_{60} chemical evolution in the NGC 7023 nebula, using Spitzer (12) and Herschel (13) infrared observations.

Observational Results

Infrared Observations of the NGC 7023 Nebula. Earlier Spitzer observations of the NGC 7023 reflection nebula have revealed a chemical evolution of PAHs: Deep in the cloud, emission is dominated by PAH clusters, which evaporate into free-flying PAHs when exposed to the UV radiation from the star (14–16). There, gaseous PAHs are, in turn, ionized. While the neutral PAHs are dominated by zig-zag edges—as demonstrated by the strong C-H solo out-of-plane modes—the ions have an armchair molecular structure, characterized by strong duo out-of-plane modes (17). In regions closest to the star, the presence of C_{60} in the neutral state is evidenced by Spitzer observations (Fig. 1). New Herschel observations provide a measurement of dust emission in the same region, at high angular resolution (Fig. 1). This measurement can be used to derive the integrated intensity radiated by the nebula, which can be used as a calibrator, to convert the Spitzer observations of the PAHs and C_{60} bands into absolute chemical abundances of these species, allowing a quantitive study of PAH and C_{60} chemical evolution.

Measurement of the Far Infrared Integrated Intensity of Dust Emission in the Nebula. The far infrared integrated intensity $I_{\rm FIR}$ was extracted by fitting the spectral energy distribution (SED) at each position in the cross-cut shown in Fig. 1. For these positions, we have used the brightnesses as measured by Herschel Photodetector Array Camera end Spectrometer (PACS) (18) and SPIRE (19) photometers. We have used the 70- and 160-μm channels of PACS and the 250-μm channel of SPIRE. This data is presented in detail in ref. 20. The modified blackbody function fit to these SEDs containing three spectral points is defined by

$$I(\lambda,T) = K/\lambda^{\beta} \times B(\lambda,T), \quad [1]$$

where K is a scaling parameter, λ is the spectral index, and $B(\lambda,T)$ is the Planck function with λ the wavelength and T the temperature. We have used a constant value of 1.8 for β so that only T and K are free parameters. The results of the fits to the observations are shown in Fig. S1. The temperatures we have derived from the fit of the data range between 25 and 30 K. These values are in agreement with those of ref. 20 for the same region. The peaking position of the modified blackbody function moves to shorter wavelengths (i.e., the grain temperature increases) when getting closer to the star, implying that we are indeed tracing matter inside the cavity and not material behind on the line of sight. The far infrared integrated intensity, $I_{\rm FIR}$, is then derived by integrating $I(\lambda,T)$ over frequencies.

Measurement of the Integrated Intensity of PAH and C_{60} Emission in the Nebula. The integrated intensity of PAH emission, $I_{\rm PAH}$, is measured by fitting a PAH emission model to the observed Spitzer midinfrared low-resolution spectrum. This data covers the 5- to 14-μm range where most of the emission occurs. Because this spectral range contains the emission due to the vibration of both C-C and C-H bonds, it is insensitive to ionization of PAHs. An example of this fitting model is presented in ref. 21. This tool provides the integrated intensity in the PAH bands as an output and takes care of continuum subtraction and extinction correction. The C_{60} integrated intensity ($I_{C_{60}}$) extraction needs to be done separately for each band. We first measure the integrated intensity in the 19- and 17.4-μm band. The first step consists in extracting the intensity in the 19.0-μm band ($I_{19.0}$) by fitting a

Author contributions: O.B. performed research; A.G.G.M.T. performed modeling; A.G.G.M.T. wrote section on dehydrogenation; O.B. analyzed data; and O.B. wrote the paper.

The authors declare no conflict of interest.

This article is a PNAS Direct Submission.

[1]To whom correspondence should be addressed. E-mail: olivier.berne@gmail.com.

This article contains supporting information online at www.pnas.org/lookup/suppl/doi:10.1073/pnas.1114207108/-/DCSupplemental.

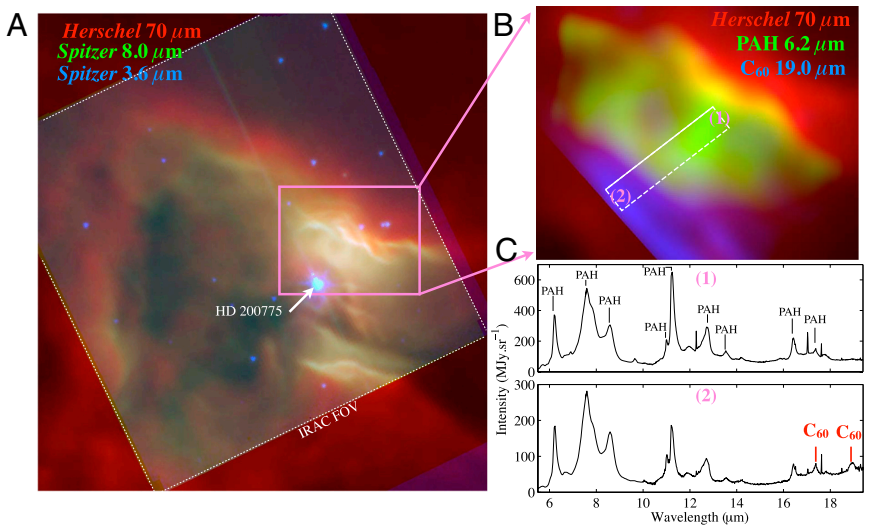

Fig. 1. Overview of the NGC 7023 nebula. (*A*) Multiwavelength color-coded view of the nebula in the infrared. Red is the emission at 70 μm observed with the Photodetector Array Camera end Spectrometer (PACS) onboard Herschel. This emission is dominated by dust. Green is the Spitzer-Infrared Array Camera (IRAC) 8-μm emission tracing the PAH C-C mode, and blue is the IRAC 3.6-μm emission, tracing the PAH C-H mode and stellar emission. The position of the intermediate mass young star HD 200775 illuminating the nebula is indicated. (*B*) Color-coded image of the spatial distribution of different compounds in NGC 7023 : Red is the emission of dust observed with Herschel-PACS, green shows the emission integrated in the 6.2 μm C-C band of PAHs observed with Spitzer-Infrared Spectrograph (IRS), and blue is the C_{60} emission observed with Spitzer-IRS integrated in the 19.0-μm band. The white rectangle shows the region on which the extraction of the PAH and C_{60} abundance (Fig. 2) was performed. (*C*) Spitzer IRS midinfrared spectra taken at positions (1) (*Upper*) and (2) (*Lower*) in *B*. The distance from the star at positions (1) and (2) are, respectively, approximately 35″ and 15″. The bands of PAHs and C_{60} are labeled in the spectra.

Gaussian and subtracting a local linear continuum. The 17.4-μm band is contaminated by PAH emission, but this can be removed effectively. The contribution of PAHs to the 17.4-μm band can be estimated in this way: In the outer regions of the nebula, the 17.4-μm band is 100% due to PAHs (because no C_{60} is detected there) and so is the 16.4-μm band. The 16.4- and 17.4-μm band of PAHs are known to correlate. Indeed, in the outer regions of the nebula we find $I_{17.4}^{\mathrm{PAH}} \sim I_{16.4} \times 0.35$. Therefore, over the whole nebula, we can estimate the intensity of the 17.4-μm band due to C_{60} by $I_{17.4}^{C_{60}} \sim I_{17.4} - I_{16.4} \times 0.35$. Fig. S2 shows the result of this process on the map. The 7.0-μm band is faint and usually hard to detect. In the regions closest to the star where both the 19- and 7.0-μm features are observed, we can calibrate the ratio of $I_{19.0}/I_{7.0}$. It is found to be relatively stable (at least in this small zone close to the star) and of the order of 0.4. Therefore, we use $I_{7.0} = 0.4 \times I_{19.0}$. The 8.5-μm band is undetectable because of the strong PAH band present at 8.6 μm, so we use the ratio provided in ref. 3 for 5 eV photons; that is, $I_{8.5} = 0.4 \times I_{19.0}$. The total C_{60} IR emission is hence given by $I_{C_{60}} = I_{19.0} + I_{17.4} - I_{16.4} \times 0.35 + I_{19.0} \times 0.4 + I_{19.0} \times 0.4$.

Derivation of PAH and C_{60} Abundances. The method to derive the abundance of carbon locked in PAHs and C_{60} from I_{PAH}, $I_{C_{60}}$, and I_{FIR} is presented in detail in ref. 22. The fraction of carbon locked in PAHs and C_{60} (respectively, $f_{\mathrm{C}}^{\mathrm{PAH}}$ and $f_{\mathrm{C}}^{C_{60}}$) per atom of interstellar hydrogen are given by

$$f_{\mathrm{C}}^{\mathrm{PAH}} = 0.23 \times \left(\frac{7 \times 10^{-18}}{\sigma_{\mathrm{uv}}^{\mathrm{PAH}}}\right) \frac{R_{\mathrm{PAH}}}{1 - (R_{\mathrm{PAH}})}, \quad [2]$$

and

$$f_{\mathrm{C}}^{C_{60}} = 0.23 \times \left(\frac{7 \times 10^{-18}}{\sigma_{\mathrm{uv}}^{C_{60}}}\right) \frac{R_{C_{60}}}{1 - (R_{C_{60}})}, \quad [3]$$

where

$$R_{\mathrm{PAH}} = \frac{I_{\mathrm{PAH}}}{I_{\mathrm{PAH}} + I_{C_{60}} + I_{\mathrm{FIR}}}, \quad [4]$$

and

$$R_{C_{60}} = \frac{I_{C_{60}}}{I_{\mathrm{PAH}} + I_{C_{60}} + I_{\mathrm{FIR}}}. \quad [5]$$

$\sigma_{\mathrm{uv}}^{\mathrm{PAH}}$ and $\sigma_{\mathrm{uv}}^{C_{60}}$ are the UV absorption cross-sections of PAHs and C_{60}. Following ref. 22, we adopt $\sigma_{\mathrm{uv}}^{\mathrm{PAH}} = 7 \times 10^{-18}$ cm^2 per C atom. There are no detailed measurements of the UV absorption cross-section of C_{60}; following ref. 3, we adopt the same value as for PAHs.

Evidence of C_{60} Formation in NGC 7023. The results of the abundance variations within the nebula as derived using the above method are shown in Fig. 2. The C_{60} abundance in the nebula is seen to increase from 1.4×10^{-4} to 1.7×10^{-2}% of the elemental carbon abundance when approaching the star (Fig. 2). On the other hand, the abundance of PAHs is seen to decrease, from 7.0 to 1.8% of the carbon (Fig. 2). This shows that C_{60} is being formed in the nebula while PAHs are being destroyed or processed. The correlation of these variations with the increasing UV field strongly suggests that UV photons control C_{60} formation and PAH processing and destruction.

The Top-Down Model

Proposed Scenario for the Formation of C_{60} in the ISM. The formation of C_{60} in the ISM is unexpected and has several implications in our understanding of the formation process of this molecule. In the laboratory, the main formation route invoked for C_{60} is the buildup from atomic carbon, small carbon clusters or rings (8–11). In space, such processes are efficient in the hot (1,500 K) and dense ($n_H > 10^{11}$ cm^{-3}) envelopes of evolved stars (6). In NGC 7023, the gas is approximately seven orders of magnitude less dense (see ref. 23 and *SI Text*), making this aggregation processes inefficient. Instead, we invoke photochemical processing of PAHs as an important route to form C_{60}. Upon UV irradiation, several channels for fragmentation can be open depending on excitation energy; e.g., H loss and C_2H_2 loss (24). However, experiments on small PAHs have shown that H loss is by far the dominant channel (25) and that complete dehydrogenation [i.e., graphene (26) formation] is then the outcome of the UV photolysis process (27, 22, 28, 29). In a second step, carbon loss followed by pentagon formation initiates the curling of the molecule (30). We envision that this is followed by migration of the pentagons within the molecule, leading to the zipping-up of the open edges forming the closed fullerene (31) (Fig. 3 and

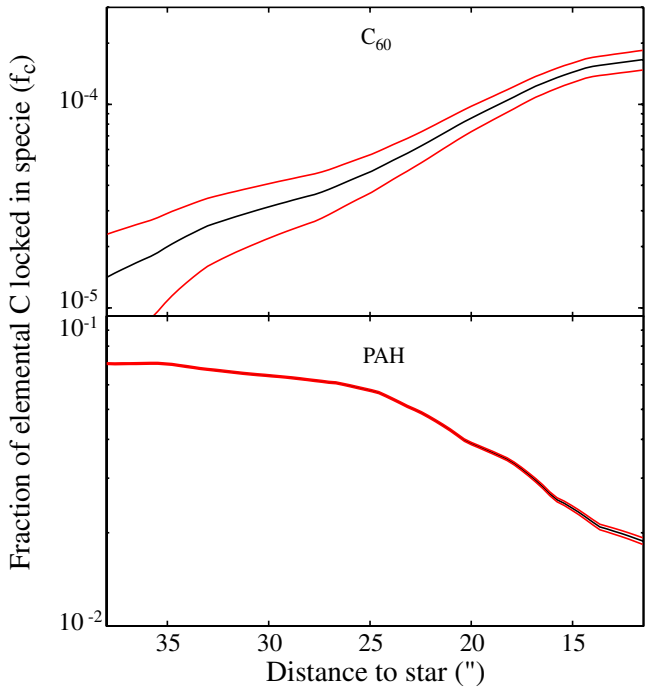

Fig. 2. Abundances of C_{60} (*A*) and PAHs (*B*) in NGC 7023 as a function of distance from the star in the cut shown in Fig. 1. The red curves give the 1 sigma uncertainty, obtained from the propagation of instrumental uncertainty on the extraction of integrated intensities of PAHs and C_{60} bands.

Movie S1). Graphene formation through PAH photolysis can give rise to a rich chemistry. Besides the route toward fullerenes outlined above, fragmentation toward small cages, rings, and chains may also result. The relative importance of isomerization and fragmentation will determine the carbon inventory delivered by the photochemical evolution of PAHs in space (Fig. 3).

PAH and Graphene Stability in Space. Guided by experimental (27) and theoretical (28) studies, we have evaluated the stability of PAHs against dehydrogenation, and C_{60} formation, in conditions appropriate for NGC 7023.

Graphene Formation

Schematically, the fragmentation process can be written as

$$\mathrm{PAH} + h\nu \leftrightarrow \mathrm{PAH}^* \rightarrow \mathrm{PAH}_{-\mathrm{H}} + \mathrm{H}, \qquad [6]$$

where PAH^* is the excited species that can stabilize through emission of IR photons or through fragmentation and $\mathrm{PAH}_{-\mathrm{H}}$ is a dehydrogenated PAH radical. There are various ways to evaluate the unimolecular dissociation rate constant for this process (compare ref. 22, section 6.4). We will follow ref. 32 and write the rate constant in Arrhenius form,

$$k(E) = k_o(T_e)\exp[-E_o/kT_e], \qquad [7]$$

where T_e is an effective excitation temperature, E_o is the Arrhenius energy describing the process, and the preexponential factor k_o depends on the interaction potential (in the reverse reaction). For PAHs, the internal excitation of the vibrational modes after the absorption of a UV photon can be well described by

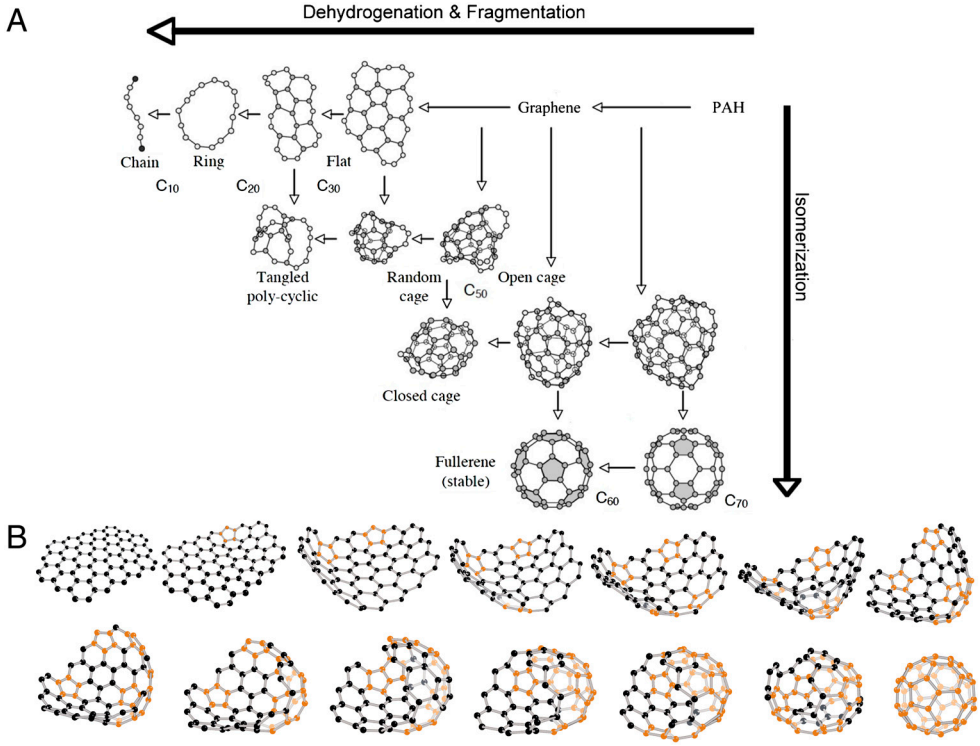

Fig. 3. Schematic representation of top-down interstellar carbon chemistry. (*A*) The chemical evolution of PAHs in the ISM under the influence of UV photons combines the effects of dehydrogenation and fragmentation with those of isomerization. Fully hydrogenated PAHs—injected by stars into the ISM—are at the top right side. Near bright stars, UV photolysis will preferentially lead to complete H loss (e.g., the "weakest link") and the formation of graphene. Further fragmentation may lead to the formation of flats, rings, and chains. However, this process competes with isomerization to various types of stable intermediaries such as cages and fullerenes. (*B*) Schematic illustration of conversion of graphene into C_{60} in 13 steps. Dehydrogenated PAHs (i.e., graphene sheets) loose carbon atoms under UV irradiation, giving rise to pentagonal defects (represented with orange C atoms) at the edges of the sheet. These defects in the hexagonal network induce curvature of the sheet, the migration of the pentagons allows the molecule to close. Image courtesy of L. Cadars (www.laurecadars.com).

$$T_m = 2{,}000\left(\frac{E(\text{eV})}{N_c}\right)^{0.4}, \quad [8]$$

where N_c is the number of C atoms and E is internal energy in eV (ref. 22, p. 184). Because typically the energy involved in these reactions is a fair fraction of the total energy in the system, a correction has to be made to this excitation temperature. The finite heat bath correction results in (22, 32)

$$T_e = T_m\left(1 - 0.2\frac{E_o}{E}\right). \quad [9]$$

The preexponential factor can be set equal to

$$k_o = \frac{kT_e}{h}\exp\left[1 + \frac{\Delta S}{R}\right], \quad [10]$$

with ΔS the entropy change for which we will adopt 5 cal/K (28). k_o is then, typically, $\simeq 3 \times 10^{16}$ s^{-1}. The Arrhenius energy parameter, E_o, cannot be easily evaluated from theoretical calculations (33). Here, we use a fit to the experimental fragmentation studies on small PAHs [<24 C atoms; (25)], which results in $E_o = 3.3$ eV (ref. 22, p. 204). The probability for dissociation depends then on the competition between fragmentation and IR photon emission,

$$p_d(E) = \frac{k(E)}{k(E) + k_{ir}(E)}, \quad [11]$$

where $k_{ir}(E)$ is the IR emission rate at an internal energy E. For a highly excited PAH, $k_{ir}(E)$ is approximately 1 s^{-1}. The total fragmentation rate is then

$$k_{\text{frag}} = p_d(E)k_{\text{uv}}(E), \quad [12]$$

where $k_{\text{uv}}(E)$ is the absorption rate of UV photons with energy, E.

The photochemically driven H loss is balanced by reactions of atomic hydrogen with dehydrogenated PAHs; namely,

$$\text{PAH}_{-\text{H}} + \text{H} \rightarrow \text{PAH} + h\nu. \quad [13]$$

The rate of this reaction has been measured to be $k_a = 1.5 \times 10^{-10}$ cm^3 s^{-1} for a number of small PAHs (28, 34). We can define the dissociation parameter, $\psi = k_a n_H / k_{\text{frag}}$. With $k_{\text{uv}} = 7 \times 10^{-10} N_c G_o$, where G_o is the flux of UV photons in units of the interstellar Habing field (35), we have $\psi \simeq 0.2 n_H / N_c G_o p_d(E)$. The hydrogen coverage of interstellar PAHs is a very sensitive function of ψ, and a small increase of ψ can change PAHs from fully hydrogenated to graphene (22, 34). This is illustrated for the circumovalene, $C_{60}H_{20}$, in Fig. S3. Thus, PAHs are fully hydrogenated if ψ is much less than 1 and fully dehydrogenated if ψ is much larger than 1. Hence,

$$\frac{G_o}{n_H} = \frac{0.2}{N_c}\left(1 + \frac{k_{ir}(E)}{k(E)}\right) \quad [14]$$

provide a critical relation for the transformation of PAHs into graphene. We have evaluated this relation assuming an absorbed UV photon energy of 10 eV (Fig. 4).

Fullerene Formation

After formation of graphene, UV photoabsorption can lead to loss of carbon from the skeleton. This fragmentation process competes with stabilization through IR photon emission. The reaction rate is again given by Eq. **7**. We adopt $\Delta S = 5$ cal/K, resulting in $k_o \simeq 3 \times 10^{-16}$ s^{-1}, but the exact value is not critical. For E_o, we have adopted the Arrhenius energy [3.65 eV (36)] derived from experiments on the C loss from small catacondensed PAHs (25). The calculated cohesive energy of carbon in graphene is much larger, 7.4 eV per C atom (37) but that refers to typically carbon inside the skeleton, and carbon at the edge will be less strongly bound. Ref. 31 finds a theoretical value of 5.4 eV for the C atoms at a zig-zag edge. Moreover, theoretical cohesive energies are not a good measure for the Arrhenius energy in unimolecular dissociation experiments (33). Given the low abundance of gas phase carbon, the reverse reaction is unimportant and the chemical lifetime [$\tau_{\text{chem}}^{-1} = k_{\text{frag}}(E)$] has to be compared to the dynamical lifetime of the region. We have evaluated this chemical lifetime for a typical internal energy of 10 eV as a function of the size of the graphene sheet, N_c, and the results are shown in Fig. 4.

Application to NGC 7023.

To evaluate graphene formation in NGC 7023, we look at PAH stability. The physical conditions in the nebula, characterized by parameters G_0 and n_H, can be obtained (*SI Text*). As shown in Fig. 4, H loss is very efficient in NGC 7023 for PAHs up to 70 C atoms. We then evaluate the timescale for the loss of C atoms by the graphene flakes and compare this to the dynamical age of the nebula for a $\simeq$70 C atom PAH (Fig. 4). It appears that if we adopt $E_o = 3.65$ eV, C loss is rapid compared to the age of the nebula.

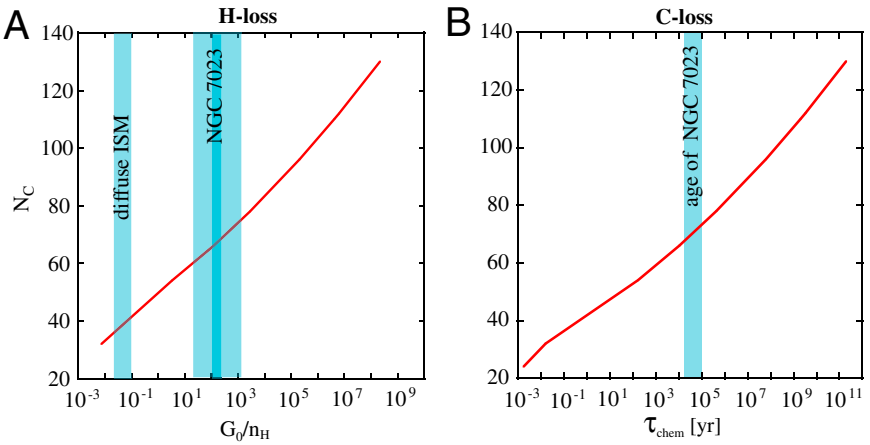

Fig. 4. Photochemistry of PAHs in NGC 7023 (*A*) The red curve shows the evolution of the critical value when PAHs have lost half of their H atoms, as a function of the physical conditions (G_0/n_H where G_0 is the radiation field in Habing units and n_H is the density of H atoms in the gas in cm^{-3}; see *SI Text* for details) and the number of carbon atoms in the PAH molecule N_C. Above this line, PAHs are stable against dehydrogenation. Below this curve, PAHs rapidly loose all their H atoms. The value of G_0/n_H for NGC 7023 is shown; dark blue represents the "narrow" range, and clear blue represents the "broad" range of values for this parameter (*SI Text*). (*B*) Timescale for the loss of a carbon atom by UV photon absorption as a function of graphene sheet size.

Discussion

Our models reveal that 70 C atoms PAH become unstable to graphene formation in the studied region of NGC 7023. Much larger PAHs will survive closer to the star, whereas smaller PAHs will rapidly be completely dehydrogenated further away, but—because of size—this will not lead to the formation of fullerenes. As shown in laboratory experiments (31), graphene sheets larger than about 70 C atoms can be transformed into fullerene, but in space this is driven by UV photons rather than energetic electrons. We surmise that fullerene formation is initiated by single C atom loss (38) at the zig-zag edge of the graphene flake. Quantum chemical calculations indeed show that the armchair structure of graphene clusters stabilizes through in plane π-bond formation, whereas the open-shell orbitals associated with the dangling bonds are located at the zig-zag edge (37), making these atoms more labile (31). A detailed study of graphene edge structure (39), based on experimental results (38), has indeed shown that single C atom loss leads to the formation of reconstructed edges bearing pentagons. These defects dramatically stress graphene flakes, inducing significant positive curvature in its topology (30). Eventually, the barrierless migration of the pentagons within the hexagonal network will lead to the zipping-up of the flake into C_{60} (31) (Fig. 3). The above mechanism is severely limited by the physical conditions, controlling dehydrogenation, and the size of the precursors, which need to be above approximately 70 C atoms. As shown by our observations, only about 1% of the available PAHs are converted into C_{60} by this process (Fig. 2). The activation of this "top-down" chemistry requires the high UV fields available near massive stars. As a corollary, high abundance of C_{60} in the diffuse ISM (40) reflects processing by massive stars, which are capable of dehydrogenating PAHs in the relevant size range (60–70 C atoms). PAHs much larger than than 70 C atoms will survive even in close encounters with massive stars. Smaller-size PAHs (<50 C atoms) cannot reach the fullerene island of stability, hence their photoprocessing (Fig. 2) must be a source of various carbon nanocompounds (45) (e.g., rings, chains, cages, bowls, tubes, etc.) (Fig. 3). Laboratory experiments have indeed shown that processing of small graphene constrictions can lead to carbon rings and chains (41). Finally, we note that recent studies suggest that PAH molecules do not provide a satisfactory explanation to the diffuse interstellar bands (42, 43). The compounds described in this top-down chemistry may be relevant to understand these features of the UV extinction curve, in the Milky Way and in other galaxies (44).

Conclusion

Analyzing infrared observations of the NGC 7023 nebula, we have found evidence that C_{60} is being formed in the ISM. Classical bottom-up formation routes fail to explain these observations, so we propose a chemical route in which C_{60} is formed directly by the photochemical processing of large PAH molecules. Other carbonaceous compounds (cages, tubes, bowls) are also the product of this photoprocessing. This route must be relevant in the ISM, but may also be important in the inner regions of protoplanetary disks around solar-type stars where accretion on the young star generates intense UV fields and PAHs are known to be present. There, they can be converted, on timescale of approximately 1 million years, into fullerenes and hydrocarbon fragments. This source of organic compounds remains to be considered in models studying the organic photochemistry of the ISM and regions of terrestrial planet formation. It is clear that such studies may benefit greatly from the progress achieved in the field of graphene stability.

ACKNOWLEDGMENTS. The authors thank the referees for their constructive comments. Laure Cadars (www.laurecadars.com) is acknowledged for producing the C_{60} formation sketch. Studies of interstellar PAHs at Leiden Observatory are supported through advanced European Research Council Grant 246976.

1. Tielens AGGM (2008) Interstellar polycyclic aromatic hydrocarbon molecules. *Annu Rev Astron Astrophys* 46:289–337.
2. Cami J, Bernard-Salas J, Peeters E, Malek SE (2010) Detection of C_{60} and C_{70} in a young planetary nebula. *Science* 329:1180–1182.
3. Sellgren K, et al. (2010) C_{60} in reflection nebulae. *Astrophys J* 722:54–57.
4. Kroto HW, Heath JR, Obrien SC, Curl RF, Smalley RE (1985) C(60): Buckminsterfullerene. *Nature* 318:162–163.
5. Goeres A, Sedlmayr E (1992) The envelopes of R Coronae Borealis stars. I—A physical model of the decline events due to dust formation. *Astron Astrophys* 265:216–236.
6. Cherchneff I, Le Teuff YH, Williams PM, Tielens AGGM (2000) Dust formation in carbon-rich Wolf-Rayet stars. I. Chemistry of small carbon clusters and silicon species. *Astrophys J* 357:572–580.
7. Pascoli G, Polleux A (2000) Condensation and growth of hydrogenated carbon clusters in carbon-rich stars. *Astron Astrophys* 359:799–810.
8. Kroto HW, McKay K (1988) The formation of quasi-icosahedral spiral shell carbon particles. *Nature* 331:328–331.
9. Heath JR (1992) Synthesis of C_{60} from small carbon clusters. *Fullerenes* pp 1–23.
10. Hunter JM, Fye JL, Roskamp EJ, Jarrold MF (1994) Annealing carbon cluster ions: A mechanism for fullerene synthesis. *J Phys Chem* 98:1810–1818.
11. Irle S, Zheng G, Wang Z, Morokuma K (2006) The C_{60} formation puzzle "solved" qm/md simulations reveal the shrinking hot giant road of the dynamic fullerene self-assembly mechanism. *J Phys Chem B* 110:14531–14545.
12. Werner MW, et al. (2004) The Spitzer Space Telescope Mission. *Astrophys J* 154:1–9.
13. Pilbratt GL, et al. (2010) Herschel Space Observatory. An ESA facility for far-infrared and submillimetre astronomy. *Astron Astrophys* 518, 10.1051/0004-6361/201014759.
14. Rapacioli M, Joblin C, Boissel P (2005) Spectroscopy of polycyclic aromatic hydrocarbons and very small grains in photodissociation regions. *Astron Astrophys* 429:193–204.
15. Berné O, et al. (2007) Analysis of the emission of very small dust particles from Spitzer spectro-imagery data using blind signal separation methods. *Astron Astrophys* 469:575–586.
16. Bréchignac P, et al. (2005) Photoinduced products from cold coronene clusters. A route to hydrocarbonated nanograins? *Astron Astrophys* 442:239–247.
17. Rosenberg M, Berné O, Boersma C, Allamandola L, Tielens AGGM (2011) Coupled blind signal separation and spectroscopic database fitting of the mid infrared PAH features. *Astron Astrophys* 532:128–142.
18. Poglitsch A, Waelkens C (2010) Geis, the photodetector array camera and spectrometer (PACS) on the Herschel Space Observatory. *Astron Astrophys* 518, 10.1051/0004-6361/201014535.
19. Griffin MJ, et al. (2010) The Herschel-SPIRE instrument and its in-flight performance. *Astron Astrophys* 518, 10.1051/0004-6361/201014519.
20. Abergel A, Arab H, Compigne M (2010) Evolution of interstellar dust with Herschel. First results in the photodissociation regions of NGC 7023. *Astron Astrophys* 518:96–100.
21. Berné O (2008) Evolution des très petites particules de poussière dans le cycle cosmique de la matière : Méthodes de séparation aveugle de sources et spectro-imagerie avec le télescope spatial Spitzer. PhD Thesis; available at http://thesesups.ups-tlse.fr/381/ (Université Paul Sabatier), pp 148–153.
22. Tielens AGGM (2005) *The Physics and Chemistry of the Interstellar Medium* (Cambridge Univ Press, Cambridge, UK).
23. Joblin C, et al. (2010) Gas morphology and energetics at the surface of PDRs: New insights with Herschel observations of NGC 7023. *Astron Astrophys* 521:25–29.
24. Ekern SP, Marshall AG, Szczepanski J, Vala M (1997) Photon-induced complete dehydrogenation of putative interstellar polycyclic aromatic hydrocarbon cations: Coronene and Naphtho[2,3-a]pyrene. *Astrophys J* 488:39–42.
25. Jochims HW, Ruhl E, Baumgartel H, Tobita S, Leach S (1994) Size effects on dissociation rates of polycyclic aromatic hydrocarbon cations: Laboratory studies and astophysical implications. *Astrophys J* 420:307–317.
26. Novoselov KS, et al. Two-dimensional atomic crystals. *Proc Natl Acad Sci USA* 102:10451–10453.
27. Joblin C (2003) Carbon macromolecules in the cycle of interstellar matter: Observational and laboratory experiments. *SF2A-2003 Semaine de l'Astrophysique Francaise*, eds Combes InF, D Barret, T Contini, and L Pagani 175–179.
28. Le Page V, Snow TP, Bierbaum VM (2003) Hydrogenation and charge states of polycyclic aromatic hydrocarbons in diffuse clouds. II. Results. *Astrophys J* 584:316–330.
29. Montillaud J, Joblin C, Toublanc D (2011) Modelling the physical and chemical evolution of PAHs and PAH-related species in astrophysical environments. 46 pp:447–452 EAS Publications Series.
30. Shenoy VB, Reddy CD, Zhang Y-W (2010) Spontaneous curling of graphene sheets with reconstructed edges. *ACS Nano* 4:4840–4844.
31. Chuvilin A, Kaiser U, Bichoutskaia E, Besley NA, Khlobystov AN (2010) Direct transformation of graphene to fullerene. *Nat Chem* 2:450–453.
32. Klots CE Thermal kinetics in small systems. *J Chem Phys* 90:4470–4472.
33. Baer T, Hase WL (1996) *Unimolecular Reaction Dynamics : Theory and Experiment* (Oxford Univ Press, Oxford).
34. Snow Theodore P, Le Page Valery, Keheyan Yeghis, Bierbaum Veronica M (1998) The interstellar chemistry of PAH cations. *Nature* 391:259–261.
35. Habing HJ (1968) The interstellar radiation density between 912 A and 2400 A. *Bull Astron Inst Netherlands* 19:421.

36. Micelotta ER, Jones AP, Tielens AGGM (2010) Polycyclic aromatic hydrocarbon processing in a hot gas. *Astron Astrophys* 510:A37.
37. Winter N, Ree F (1998) Carbon particle phase stability as a function of size. *J Comp Mat Des* 5:279–294.
38. Girit C, et al. (2009) Graphene at the edge. *Science* 323:1705–1708.
39. Koskinen P, Malola S, Häkkinen H (2009) Evidence for graphene edges beyond zigzag and armchair. *Phys Rev B* 80:73401–73404.
40. Foing BH, Ehrenfreund P (1994) Detection of two interstellar absorption bands coincident with spectral features of C_{60}^{+}. *Nature* 369:296–298.
41. Chuvilin A, Meyer JC, Algara-Siller G, Kaiser U (2009) From graphene constrictions to single carbon chains. *New J Phys* 11:83019.
42. Xiang FY, Li A, Zhong JXA (2011) A tale of two mysteries in interstellar astrophysics: The 2175 Å extinction bump and diffuse interstellar bands. *Astrophys J* 733:91–100.
43. Steglich M, Bouwman J, Huisken F, Henning T (2011) Can neutral and ionized PAHs be carriers of the UV extinction bump and the diffuse interstellar bands? eprint arXiv:1108.2972.
44. Li A, Chen JH, Li MP, Shi QJ, Wang YJ (2008) On buckyonions as an interstellar grain component. *Mon Not R Astron Soc* 390:39–42.
45. Pety J, et al. (2005) Are PAHs precursors of small hydrocarbons in photo-dissociation regions? The Horsehead case. *Astron Astrophys* 435:885–899.

Supporting Information

Berné and Tielens 10.1073/pnas.1114207108

SI Text

1 Physical Conditions in NGC 7023. ***1.1 General properties.*** NGC 7023 is a widely studied photodisociation region. We briefly review the information on physical conditions available in the literature. The nebula has an hourglass-shaped, low-density cavity, which was opened in the dense molecular cloud by the winds of the young Be star (1). The formation of C_{60} is seen to occur inside this cavity (See Fig. 1 in the main text) in regions particularly close to the star (10″ to 40″). In the next sections we discuss the values we adopt for radiation field and gas density in the cavity.

1.2 Radiation field. The intensity of the radiation field in the cavity, G_0, can be derived based on the spectral type and flux of the star diluted by the square of the distance from the star. Doing this exercise, Joblin et al. (2) find that the radiation field is $G_0 =$ 2,600 at a distance of 40″ from the star [similar to the value found by Rogers et al. (3) and Chokshi et al. (4). Using this value and spherical dilution, we derive the range of radiation fields covered in the cut where we study C_{60} and polycyclic aromatic hydrocarbon (PAH) evolution (Figs. 1 and 2). We find $G_0 = 3.0 \times 10^4$ at the peak of C_{60} abundance (12″ from the star) and $G_0 = 3.4 \times 10^3$ at the minimum of C_{60} abundance (35″ from the star). Fuente et al. (5) have reported the highest value of radiation field in the photodissociation region (PDR) with $G_0 = 1 \times 10^4$ at the position of the H_2 filaments at 46″ from the star. This would correspond to values of $G_0 = 1.7 \times 10^4$ and $G_0 = 1.5 \times 10^5$ at the edges of the cut (respectively, 35″ and 12″ from the star). We therefore adopt average values $G_0 = 1.0 \pm 0.7 \times 10^4$ and $G_0 = 1.0 \pm 0.7 \times 10^5$ at 35 and 12″ from the star.

1.3 Density in the cavity. The density of the atomic gas in this region is difficult to derive directly, but can be constrained from observations of the surrounding molecular cloud. More specifically, the density derived from CO lines by Gerin et al. (6) in the back wall of the cavity point to a value of $n_H^{\mathrm{Mol}} \sim 3{,}000$ cm^{-3}. The atomic gas well within the cavity, is expected to be at least an order of magnitude hotter, and hence an order of magnitude less dense if we consider pressure equilibrium (i.e., $n_H^{\mathrm{Cav}} \sim 300$). Rogers et al. (3) find that $n_H^{\mathrm{Mol}}/n_H^{\mathrm{Cav}} = 10^{-35}$, which then implies $n_H^{\mathrm{Cav}} =$ 85–300. Joblin et al. (2) quote a value of 100 cm^{-3} for n_H^{Cav}. A more direct estimation of the column density of warm atomic gas can be derived from the dust emission. Because we have seen that dust temperature increases when getting closer to the star (see first section of this document), this implies that this emission indeed comes form the cavity and not from the wall behind. Using the DUSTEM (7) model, we can reproduce the observed emission in the Photodetector Array Camera end Spectrometer 70-μm filter at a distance of 35″ from the star (approximately 1 Jy/pixel or 2,300 MJy.sr^{-1}), for a radiation field of $G_0 = 10^4$, and leaving the column density as a free parameter. This yields $N_H = 2 \times 10^{19}$ cm^{-2} for the cavity, which with a physical size of 5.7×10^{17} cm ($2 \times 35''$ at 400 pc) corresponds to $n_H^{\mathrm{Cav}} = 45$ cm^{-2}, somewhat lower than other estimates based on PDR or molecular tracers. Note that this determination does not depend significantly on the accuracy of determination of radiation field in the considered range of G_0 (see ref. 7, figure 7). We keep $n_H^{\mathrm{Cav}} = 50$ as lower limit and $n_H^{\mathrm{Cav}} = 250$ as upper limit and adopt $n_H^{\mathrm{Cav}} = 150 \pm 100$ cm^{-3}.

1.4 G_0/n_H. Using the adopted average density and radiation field values we can obtain G_0/n_H needed to estimate the dehydrogenation efficiency (see *Graphene Formation* in the main text). We find $G_0/n_H = 65 \pm 45$ at 35″ from the star and $G_0/n_H = 650 \pm 450$ at 12″ from the star. From these numbers, we define the "broad" and "narrow" domains of values of G_0/n_H expected in the cut in NGC 7023, [20–1100] and [105–200], respectively. These are represented graphically in Fig. 4 over the dehydrogenation stability curve.

1. Fuente A, Martin-Pintado J, Bachiller R, Neri R, Palla F (1998) Progressive dispersal of the dense gas in the environment of early type and late-type Herbig Ae-Be stars. *Astron Astrophys* 334:253–263.
2. Joblin C, et al. (2010) Gas morphology and energetics at the surface of PDRs: New insights with Herschel observations of NGC 7023. *Astron Astrophys* 521:25–29.
3. Rogers C, Heyer MH, Dewdney PE (1995) H I, CO, and IRAS observations of NGC 7023 *Astrophys J* 442:694–713.
4. Chokshi A, Tielens AGGM, Werner MW, Castelaz MW (1988) C II 158 micron and O I 63 micron observations of NGC 7023—A model for its photodissociation region *Astrophys J* 334:803–814.
5. Fuente A, et al. (1999) Infrared Space Observatory observations toward the Reflection Nebula NGC 7023: A nonequilibrium ortho-to-para-H_2 ratio. *Astrophys J* 518:45.
6. Gerin M, Phillips TG, Keene J, Betz AL, Boreiko RT (1998) CO, C I, and C II observations of NGC 7023 *Astrophys J* 500:329.
7. Compiègne M, et al. (2011) The global dust SED: tracing the nature and evolution of dust with DustEM. *Astron Astrophys* 525:103.

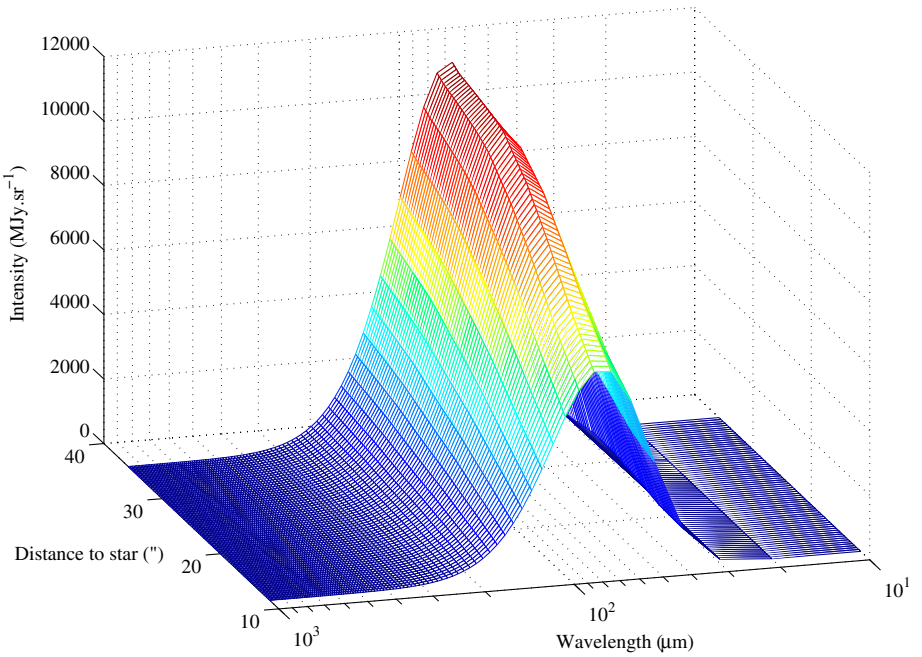

Fig. S1. Fitted modified black bodies to the SEDs observed with Herschel in the cross-cut from position (1) to (2) shown in Fig. 1.

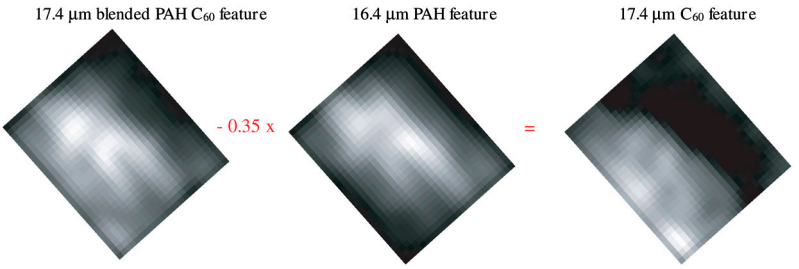

Fig. S2. Subtraction of the contamination of PAHs in the 17.4-μm band.

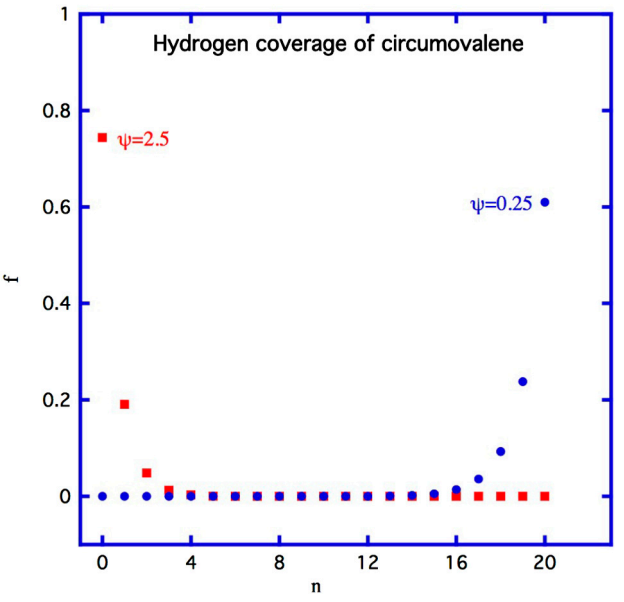

Fig. S3. The relative abundance of circumovalene and its partial dehydrogenated derivatives, $C_{66}H_n$, for two values of the dissociation parameter, ψ.

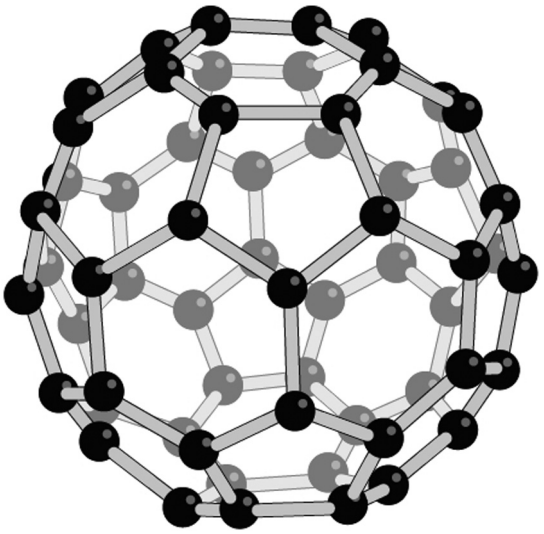

Movie S1. Conversion of graphene into C_{60}. This video shows schematically how graphene can be converted into C_{60}. We start with a sheet of graphene where carbon atoms are arranged in a hexagonal network. Under UV irradiation, C atoms are lost in the hexagons situated at the edge of the graphene flake and converted into pentagons (shown in orange). The formation of pentagons stresses the molecule forcing it to curve. When several pentagons have been formed, they can migrate inside the molecule. Finally, when 12 pentagons have been formed and when each carbon atom belongs to both a pentagon and a hexagon, the molecule closes into C_{60}.

Movie S1 (MOV)